Surface & Coatings Technology 206 (2012) 4791–4798

Contents lists available at SciVerse ScienceDirect

Surface & Coatings Technology

journal homepage: www.elsevier.com/locate/surfcoat

Chemical and mechanical properties of anodized cp-titanium in NH_4 H_2PO_4/NH_4F media for biomedical applications

Lucas Aloia Games [a], Andrea Gomez Sanchez [a], Emilio Jimenez-Pique [b], Wido H. Schreiner [c], Silvia M. Ceré [a], Josefina Ballarre [a,*]

[a] Material's Science and Technology Research Institute (INTEMA), UNMdP-CONICET Juan B. Justo 4302, B7608FDQ, Mar del Plata, Argentina
[b] Departament de Ciència dels Materials i Enginyeria Metallúrgica, Universitat Politècnica de Catalunya, Avda. Diagonal, 647 (ETSEIB), 08028 Barcelona, Spain
[c] LSI-LANSEN, Departamento de Física, UFPR, CP 19081, 81531-990, Curitiba, Brazil

ARTICLE INFO

Article history:
Received 20 December 2011
Accepted in revised form 30 March 2012
Available online 9 April 2012

Keywords:
Anodizing
Titanium
Phosphor-compounds
Adhesion
Nanoindentation

ABSTRACT

Potentiostatic anodizing of commercially pure titanium, using ammonium phosphate and ammonium fluoride solution as electrolyte is studied. The objective is to generate titanium oxides on the surface and phosphor compounds presenting good protective and mechanical properties, and proper adhesion to the metal substrate to remain during surgical orthopedic procedures (implants). Two different applied potentials were used to obtain different surface oxides morphologies (20 and 30 V). The characterization and quantification of the generated deposits is presented as a starting point for the future application of these composite types of materials. X-ray Photoelectron Spectroscopy (XPS) and Raman spectroscopy techniques showed the presence of phosphor compounds and anatase (TiO_2) as the main constitutive phases.
Anodized samples presented less passivity current density with respect to the bare substrate, showing that the film formed by anodizing acts as an effective barrier to the electrolyte entrance to reach the metallic surface. Besides, mechanical properties of bare substrate were improved with the formation of anodic films: hardness value was increased in the oxide zones and the Young's elastic modulus was decreased in the phosphor-compounds zones in the sample anodized with 30 V, generating an interface with different elastic properties that could be able to enhance the prosthesis performance. Nano-scratch tests showed a very ductile behavior and good adhesion of anodic films, without any apparent signs of cracks or delamination.

1. Introduction

Metallic materials are widely used as orthopedic and odontologic surgical implants due to their excellent mechanical properties and the controlled corrosion resistance that some of them present for these applications [1]. A disadvantage of prosthetic metallic materials is that most of them cannot make a natural bonding with the existing tissue, therefore a chemical or mechanic fixation is necessary. Also the material that is going to be implanted should have good wear resistance, since materials could also release metallic particles to the surrounding media, causing different pathologies that could finally lead to the removal of implant [2].

The use of titanium as permanent implant material is widely known in orthopedic and dentistry field. The reduced ion release and excellent biocompatibility is largely attributed to the spontaneous formation of an inert surface passive film of non-stoichiometric TiO_2, typically 4–10 nm thick, which is amorphous and poorly crystallized [3,4]. Oxidation and electrochemical methods can modify surface oxide properties of implants, such as oxide thickness, chemical composition, crystal structure, porosity or pore structure, density and roughness [5]. Among the surface oxide properties of the oxidized implants, the surface chemistry of the oxide generated layer has been thought to influence bone response [6,7]. Several types of TiO_2 films generated by some electrochemical or electric method are used nowadays to generate compact, controlled and adherent oxides [8–11] The formation of nano-structured titanium oxide layer (sometimes as nanotubes) was observed to be environment specific [10,12–15]. The need of fluorine ions to form a porous-controlled structure has been reported by Beranek et al. [16] where they proposed a growth-dissolution mechanism of the film formation. Sul et al. [17] support that oxide generated films with thickness larger than 600 nm, provide better implant performance *in vivo*. This better performance was related to the oxide thickness *per se*, differences in surface oxide morphology (porous compact barrier in native oxides *vs.* porous oxide structure with porosity of 13–24%), the difference between crystal structure of amorphous oxide in native oxides and a mixture of amorphous, anatase and rutile phases, and differences in surface roughness [17]. The characterization of the oxides present in the surface and its quantification are key issues for the future calcium phosphate deposition (apatite, first insight of bone formation [18]) in order to provide bioactivity and further mechanical fixation.

* Corresponding author at: Juan B. Justo 4302, B7608FDQ, Mar del Plata, Argentina. Tel.: +54 223 481 6600; fax: +54 223 4810046.
E-mail address: jballarre@fi.mdp.edu.ar (J. Ballarre).

0257-8972/$ – see front matter © 2012 Elsevier B.V. All rights reserved.
doi:10.1016/j.surfcoat.2012.03.092

Superficial features, such as elastic modulus, hardness, friction coefficient and adhesion of the generated deposits to the metallic substrate, and their mechanical properties, are of great importance since they are subjected to several mechanical efforts during and after implantation. In regard to the mechanical and elastic properties, the interface between the implant and the existing bone should change gradually. Instrumented indentation, also known as nanoindentation when the resolution of the instrument is in the nanometer range, is one of the most recent techniques used to study the mechanical properties of thin films. In this technique, a load is applied to an indenter and the displacement into the material is recorded simultaneously. Analysis of the load (P)–penetration (h) curves allows the calculation of mechanical parameters, mainly hardness and elastic modulus, without the need of visualizing the imprint. With a lateral force modulus, and a ramped load in a displacement (scratch) path, a nano-scratching test can be done on the sample surface [19–23].

The aim of this work is to advance in the understanding of surface modification of commercially pure titanium implants, used in orthopedic surgery and dentistry, through a potentiostatic anodizing surface treatment. The process is carried out in an ammonium phosphate and ammonium fluoride solution in order to generate a P-rich rough, adherent and protective film on titanium substrate. The chemical, electrochemical, adhesive and mechanical characterization of the formed deposits after the anodizing process is presented as an important starting point for further implementation of these materials.

2. Experimental procedure

2.1. Substrates and anodizing treatment

Samples of $28\times13\times0.3$ mm^3 grade-2 commercially pure Titanium sheets (cp-Ti,) were employed. Its chemical composition is (wt.%): Ti 99.2, C 0.1 max, Fe 0.3 max, H 0.01 max, N 0.03 max and O 0.25 max. The initial surface conditioning was performed by polishing with 600 grit paper using water as lubricant.

Anodizing treatment samples were cleaned in ultrasonic bath with acetone during 10 min and followed by a bath with isopropylic alcohol for another 10 min. The electrolytic solution was prepared with bi-distillated water, 1 mol.L^{-1} of NH_4 H_2 PO_4 and 0.135 mol.L^{-1} of NH_4 F both from Sigma Aldrich.

Anodizing treatment was carried out with a Power source Consort EV231 (Belgium) in a two-electrode cell. The auxiliary electrode was a stainless steel mesh that acts simultaneously as a reference electrode. The specimens were anodized in the electrolytic solution at a constant potential of either 20 V or 30 V with respect to the reference electrode, for 60 min at room temperature. These samples will be referred to in the rest of the manuscript, as *AP20* and *AP30* for the 20 V and 30 V anodizing treatment respectively. Before and after each test, samples were cleaned with acetone, dried in air and stored in a dryer.

2.2. Surface characterization

Scanning electronic microscopy (SEM, JEOL JSM 6460LV, Japan) was used for the morphologic evaluation of the surface deposits. Raman spectroscopy essays were done with the aim of identifying different compounds present in the surface. Raman characterization was held in an Invia Reflex confocal (Reinshaw, UK) with a 514 nm wave length laser, at 100% intensity in a window from 100 to 1500 cm^{-1}, with one accumulation and 50 s exposition per spectrum.

X-ray photoelectron spectroscopy (XPS) essays were performed with base pressure in the experimental chamber, lower than 10^{-9} mbar. The spectra were collected using Mg Kα (1253.6 eV) radiation and an overall energy resolution of about 0.8 eV. Survey spectra were recorded for the samples in the 0–1100 eV kinetic energy range by 1 eV steps. High resolution scans with 0.1 eV steps were conducted over regions of interest: Ti 2p, F 1 s and P 2p. In all cases, surface charging effects were compensated by referencing the binding energy (BE) to the C 1 s line of residual carbon set at 284.5 eV BE [24]. Spectral decomposition assumed mixed Gaussian–Lorenzian curves. Focused Ion Beam (FIB) cross sections were made in a Neon Zeiss 40 microscope equipped with FE-SEM column (Germany), by milling with a Ga beam at 30 kV with decreasing current intensities up to a final polishing at 150pA. Finally, surface roughness of the samples was measured with a profilometer Taylor–Hobson Surtronic + 3 (Taylor Hobson, UK, vertical resolution 0.01 μm) taking the average of six zones of each sample.

2.3. Electrochemical characterization

A simulated body fluid (SBF) solution was used as electrolyte in all experiments. SBF was prepared with the following chemical composition [25]: NaCl (8.053 g.L^{-1}), KCl (0.224 g.L^{-1}), $CaCl_2$ (0.278 g.L^{-1}), $MgCl_2.6H_2O$ (0.305 g.L^{-1}), K_2HPO_4 (0.174 g.L^{-1}), $NaHCO_3$ (0.353 g.L^{-1}), $(CH_2OH)_3$ CNH_2 (6.057 g.L^{-1}). Concentrated hydrochloric acid (HCl) was added to adjust the pH to 7.30 ± 0.05.

Electrochemical essays were carried out in a Gamry Reference 600 (Gramry, USA) electrochemical unit with a conventional three electrode cell. The reference electrode was a saturated calomel electrode (SCE, Radiometer Copenhagen), a platinum wire as a counter electrode and Ti samples as working electrode. Potentiodynamic polarization curves were conducted from the corrosion potential (Eoc) to 1 V and backwards, or up to a maximum current density of 0.001 A.cm^{-2}, at a sweep rate of 0.002 V.s^{-1}.

2.4. Mechanical characterization

The mechanical elastic–plastic properties of the phosphor-oxide layers on Ti substrates were studied using the nanoindentation technique. Both, Young's modulus and hardness were determined from the load–displacement curves by the Oliver and Pharr method [26]. A Nanoindenter XP (MTS Nano Instruments) with a continuous stiffness module (CSM) was used, allowing the continuous measurement of contact stiffness (S) and load (P) as a function of penetration depth (h). Indentations were made to a maximum depth of 2000 nm (to a maximum load between 160 and 190 mN), and under a constant deformation rate of 0.05 s^{-1} for all measurements. A Poisson ratio of 0.25 was assumed for the systems. A three-side pyramid Berkovich indenter was used and it was calibrated against fused silica standard. Multiple indentations (a matrix of 4×4) separated by 100 μm were made in each sample in order to obtain average values.

Hardness was estimated by the values obtained at 1/10 of the penetration depth, while in the case of Young's modulus, it was extrapolated to estimate the values of the coatings.

Nano-scratch tests were performed using a nano-indenter XP, MTS NanoInstruments (MTS Nano Instruments, US) (force resolution: 50 nN; displacement resolution: 0.1 nm) equipped with a nano-scratch attachment that allows lateral force measurements. A pyramidal diamond Berkovich indenter was used to scratch each coating/substrate system and a 700 μm scratching track was applied in all tests. At first (pre-scan step), the tip approaches the surface under default conditions, then the load is maintained (0.1 mN) through all the scratch distance (100 μm initial + 500 μm straightforward scratch + 100 μm final). An initial surface profile of the samples is made before scratching. In the second step (scratching), the tip starts scratching at 100 μm from the start point with a ramped load (final maximum applied load of 200 mN) to the distance of 600 μm, corresponding to an effective scratch distance of 500 μm, where the load is removed to the initial one (0.1 mN) and maintained constant for 100 μm more. In all cases, the scratch testing was done with one of the edges of the Berkovich tip pointing in the direction of the scratch. The surface profile could be sensed by the depth-sensing system. In the third step (post-scan), the test is done in the same way described in the pre-scan step, in order to measure the elastic recovery after scratching.

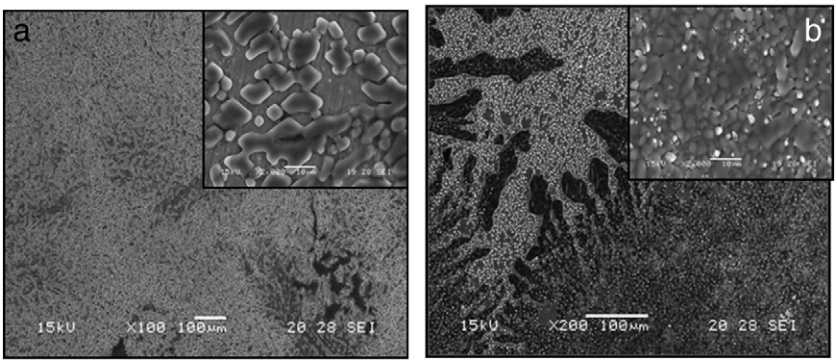

Fig. 1. Scanning Electronic Microscopy (SEM) images corresponding to the titanium anodized samples with the two analyzed applied voltages: (a) 20 volts (*AP20*) with and image magnification in the up right corner; and (b) 30 volts (*AP30*) with also am image magnification in the up right corner.

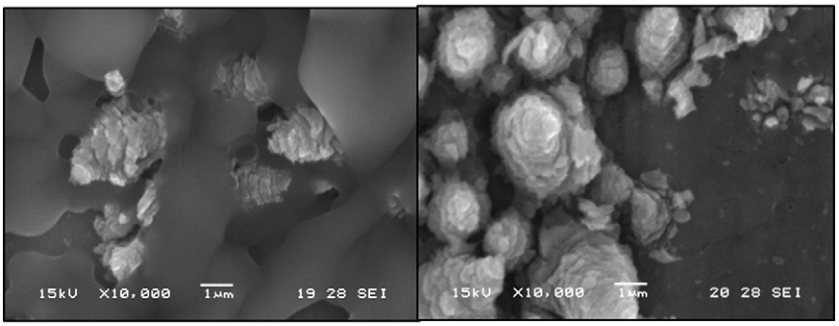

Fig. 2. SEM images of the *AP30* sample, showing in detail the spherical-shape white deposits.

Lateral (friction) forces were calculated from the deflexion of the loading column. The coefficient of friction (COF) was calculated by taking the ratio of the lateral force and the normal load applied on the indenter afterwards [27].

3. Results and discussion

In Fig. 1 the SEM images corresponding to the anodized samples can be observed. A high amount of cloud-like deposits can be identified over the entire surface of both samples. The *AP30* sample (Fig. 1(b)) presents a distinctive characteristic: some spherical-shape white deposits over the cloud-like deposits. From an amplified image, a rosette-like shape, typical from titanium oxide growth, can be observed (Fig. 2) [28,29].

The mechanical modification of the surface due to the polishing procedure in general, is thought to generate a smooth surface and to provide an energetic and plane surface to enhance the oxide growth [30]. The surface roughness measured with profilometry of the polished sample has a Ra = 0.100 ± 0.009 µm. Comparing with the Ra values measured for the polished samples without anodizing, *AP20* has a value of 0.212 ± 0.052 µm and the *AP30* presented Ra values of 1.096 ± 0.049 µm, denoting that the deposits on the 30 V sample enhance the heterogeneity of the surface. From the morphological comparison of the different deposits on titanium substrates, it can be noted that the final surface roughness and the applied voltage highly influences the shape, distribution, quantity and quality of the deposits.

At intermediate potentials, several authors agree with the presence of crystalline forms of titanium dioxide anatase and rutile with a certain degree of crystallinity [31,33], however this was not seen at the so called rupture potential [32], when the formation of amorphous thin layers of titanium oxides can be denoted. This effect was not observed in the present work with XRD essays: the rutile and anatase phases were not clearly denoted. This could be due to the heterogeneity of the layers or to the incapacity of the diffraction method to detect enough amounts of them. The presence of titanium oxide with anatase as main crystalline phase can be clearly denoted by Raman analysis (Fig. 3) in all samples. The *AP30* spectrum shows the presence of some characteristic peaks of the anatase phase in 144–148, 400, 516 and 640 cm^{-1}. The rutile phase peaks are not present (624–632, 445–447 and 236–238 cm^{-1}). The inability to detect rutile peaks can be due to their proximity to the anatase peaks, because they are not present, or because they are present in very small amounts [32,34]. Phosphor-compounds related with phosphates salts, can also be identified in the samples at 925 and 340 cm^{-1} [35], with a clear presence in the *AP20* sample. Although

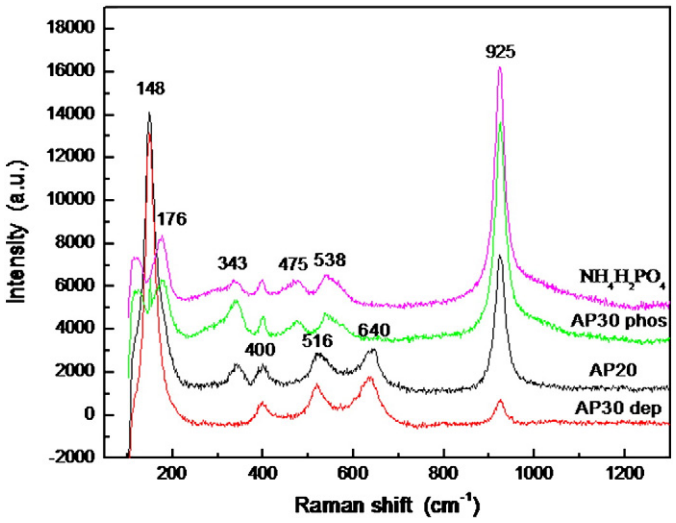

Fig. 3. Raman Spectroscopy spectra of the anodized samples (*AP20* and *AP30* in different zones) and the ammonium phosphate salt. The position of the main peaks found was added.

they are present in both samples, they are present in a larger amount at the *AP20* sample, as can be denoted by the increase in intensity of the 925 cm^{-1} peak (assigned to symmetric PO_4 stretching mode), and by the presence of the 340 cm^{-1} peak (assigned to bending vibration of O–P–O linkages).

Fig. 4(a)–(c) present the high resolution XPS scans for Ti 2p, P 2p and F 1 s regions, for all conditions under study respectively. The presence of metallic titanium was not observed for the anodized samples and only the characteristic peaks of Ti^{4+} were denoted. The amount of titanium oxide seems to be greatest (largest area under the curve) in the *AP30* sample. All of the anodized samples presented phosphor on the surface, with an energy binding of 133.3 eV, corresponding to some phosphate ($-PO_4$) or pyrophosphate ($-P_2O_7$) species [36] coming from the anodizing solution. The influence of ammonium fluoride present in the anodizing solution could be identified by the F 1 s peak in the XPS spectra (Fig. 4(c)). The anodized samples presented F 1 s signal at 685.5 eV, corresponding to F^- chemically adsorbed on the Ti/TiO_2 surface [37]. The effect of fluoride ions in the anodizing solution is widely studied and is used to chemically attack the surface and to obtain certain distribution of oxides at the surface of the metal [38,39]. The fluoride ions could be associated with the titanium oxide formation with the 30 V of applied voltage.

Fig. 5 shows the potentiodynamic polarization curves for the untreated and anodized samples at the two applied voltages (20 and 30 V). It can be observed that the anodic film acts as an effective barrier to the electrolyte entrance to reach the metallic surface in all treated samples, showing less passivity current density respect to the bare substrate. For the bare titanium at the corrosion potential zone, a pseudo-active region is observed where the oxide layer is formed and then a passive zone is reached for more than 1 V range. Both anodizing samples *AP20* and *AP30* show a two-step active/passive curve behavior. The first current density raise could be related with the chemical dissolution of anodic generated layer with the help of the F content [28]. Then the porous structure begins to assemble

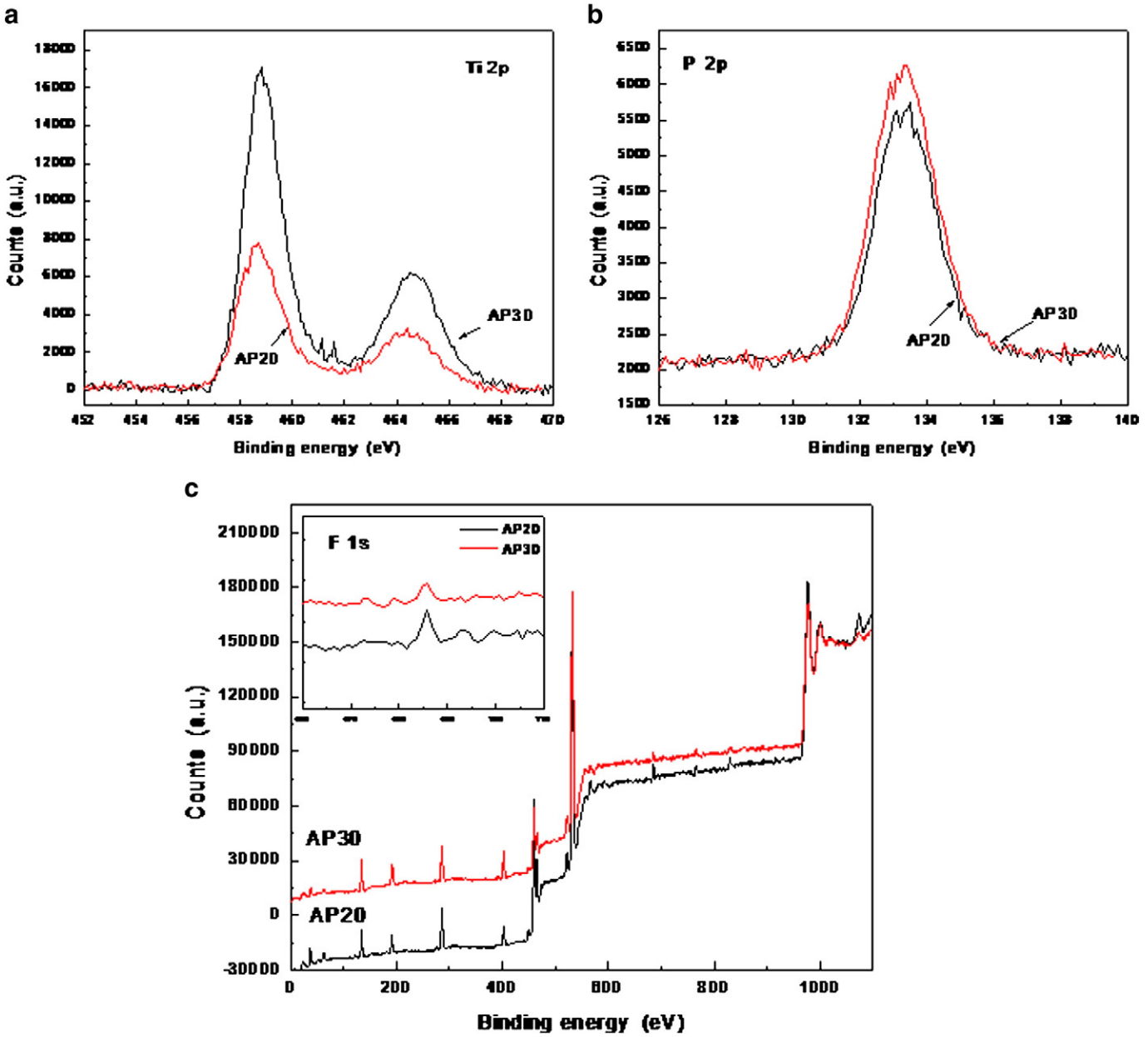

Fig. 4. Survey and high resolution X-ray Photoelectron Spectroscopy scans of the two types of anodized titanium samples: with 20 volts applied voltage (*AP20*) and with 30 volts (*AP30*). The studied regions are for the: (a) Ti 2p; (b) P 2p; and (c) F 1s.

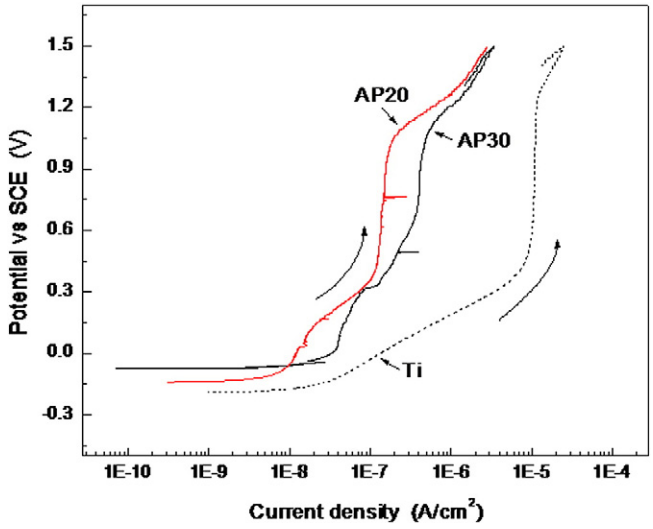

Fig. 5. Potentiodynamic polarization curves for the untreated (– – - Ti) and anodized samples at the two applied voltages (— AP20 and — AP30) in simulated body fluid.

Table 1
Electrochemical parameters obtained from the potentiodynamic experiments of the anodized titanium samples (*AP20*, *AP30*) and the bare material.

	Eoc (V)	i_{pass1} (A/cm^2)	i_{pass2} (A/cm^2)
Ti-cp	-0.28 ± 0.1	$1.1\times10^{-5}\pm1\times10^{-6}$	–
AP20	-0.11 ± 0.08	$2.4\times10^{-8}\pm1\times10^{-8}$	$2.2\times10^{-7}\pm7\times10^{-8}$
AP30	-0.08 ± 0.02	$7.8\times10^{-8}\pm3\times10^{-8}$	$6\times10^{-7}\pm2\times10^{-7}$

and the passivity is restored. No breakdown or pit potential has been observed. Table 1 shows the open circuit potential (E_{oc}), the first passivity current density (i_{pass1}) and the second passivity current density (i_{pass2}), in order to electrochemically compare the performance of the anodized samples with the bare material.

Fig. 6(a) illustrates by optical microscopy the general indented surface of the *AP20* sample where the mechanical essays took place. Fig. 6(b) represents the hardness (H) *vs.* penetration depth for the same sample. The change in the slope orientation determines the Y-axis point when an approximate value of the film thickness can be read. Fig. 7 shows SEM-FIB images of the *AP20* condition where a surface's profile with the Berkovich indentation is clearly distinguished, and also the thickness of the coating can be estimated. On other hand, the surface morphology of the *AP30* sample, as was shown in Fig. 2, is very irregular due to the spherical titanium oxide deposits and showed two distinctive zones: one related to the deposition of a smooth layer on the Ti substrate, and the other one with the growth of oxide rosettes. Fig. 8 illustrates the Young's modulus and hardness *vs.* penetration depth for the analyzed sample. In the area of the *AP30* corresponding to the phosphate deposits, values of Young modulus and hardness increase when the indenter penetrates into the layer. This event can be related with a densification of the phosphate film due to the applied pressure. A plateau is reached at 600 nm with the stabilization of mechanical properties. In both zones of this *AP30* sample at the maximum applied load/displacement, the substrate is not reached and it does not affect the measured values. Also SEM-FIB images were taken from the rosettes zone at the *AP30* sample. In Fig. 9 the open layered structure of the oxide deposits can be seen as well as their thickness. For the phosphate zone, the thickness estimation is less than 1 μm and for the rosettes zone is more than 3 μm.

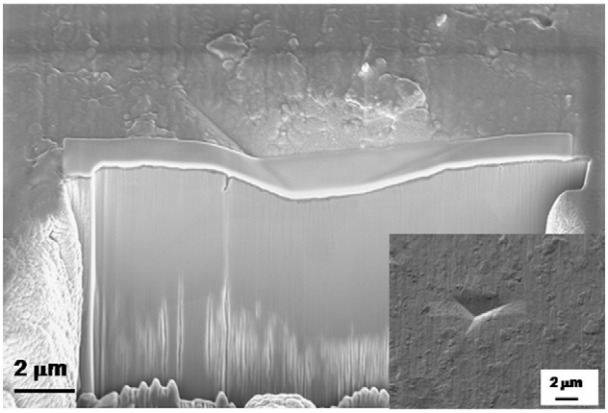

Fig. 7. SEM-FIB images of the *AP20* condition where a surface's profile with the Berkovich indentation can be observed.

The mean value of the Young's modulus (E) and the hardness (H) with the corresponding standard deviation were calculated employing the continuous stiffness data for the bare titanium, *AP20* and *AP30* samples (Table 2). Hardness values were taken at 70–150 nm of penetration depth of the deposited coatings for the *AP20* and at 200–300 nm for the *AP30* sample, since it is assumed that at 1/10 of the thickness of the film, this value is not influenced by the substrate

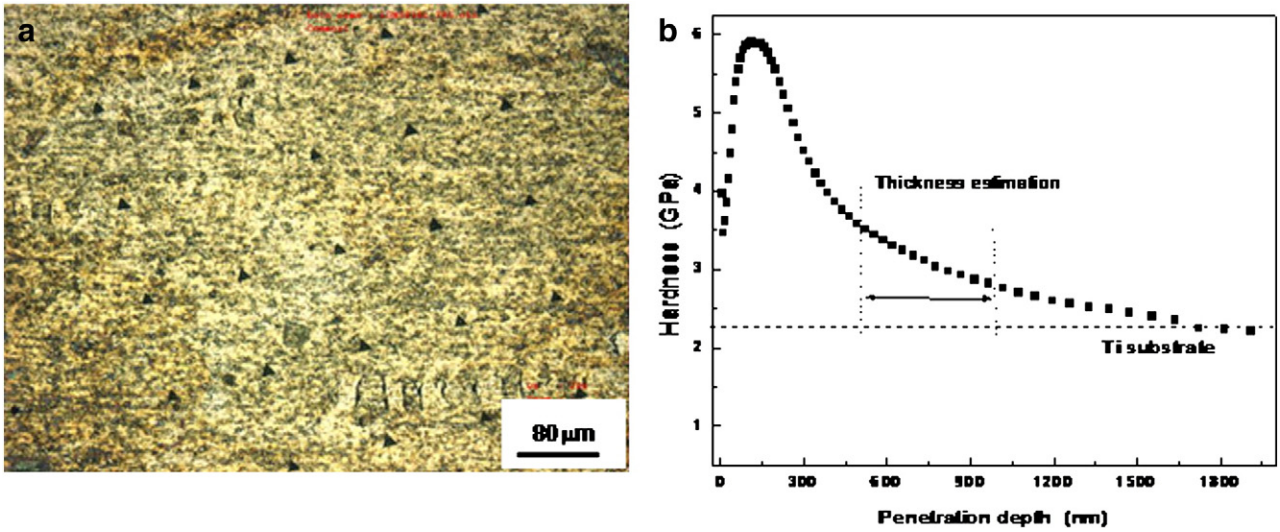

Fig. 6. (a) Optical microscopy image of the anodized titanium sample with 20 volt treatment showing the surface after indentation. (b) Graph of the obtained Hardness vs. Penetration depth of the indenter on the anodic layer for the same sample (*AP20*).

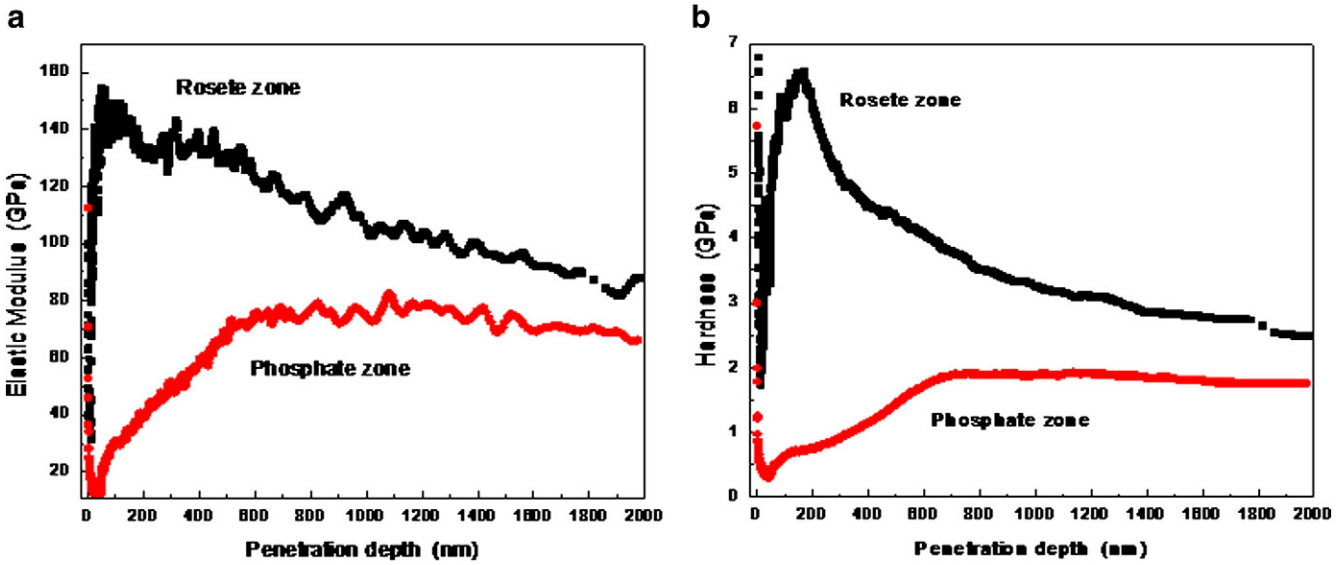

Fig. 8. Graphs showing calculated (a) Elastic Modulus vs. Penetration depth and (b) Hardness vs. Penetration depth into the deposited layers formed with the 20V (*AP20*) and the 30V treatment on polished titanium.

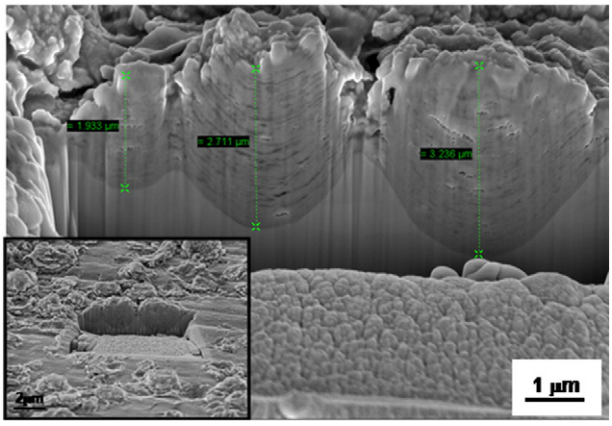

Fig. 9. SEM-FIB images of the *AP30* sample where the shape and growth of the rosette-like deposits can be distinguished.

[40]. Young's modulus was extrapolated to zero thickness in order to estimate the value of the anodic films [41]. No thin film models were used as the roughness of the sample resulted in a large scatter.

The flawless state of every coated system is quite important for biomedical applications in order to avoid corrosion or wear events. In all samples analyzed no film cracking was observed after indentation. However, it has to be noted that low loads were applied.

The adhesive and frictional behavior of the two types of anodizing treatment performed, were analyzed with the results of the nanoscratch tests, searching for delamination or plowing events and trying to qualify the adhesive behavior of the films. Fig. 10 shows the surface profiles and the optical images of the *AP20* and *AP30* systems, respectively. The scratch depths (nm) are plotted as a function of the horizontal displacements (µm). The curves illustrate the sample behavior during the pre-scan, scratching and post-scan test steps. The initial scan at a continuous application of low load is done to analyze the roughness of the film surface. This profile is used in relation to the post-scan in order to evaluate surface damage, adhesion and elastic–plastic deformation after the scratching process. Negative depths correspond to the scratch indenter being pushed into the film, while positive depths indicate outward blistering of the surface or the accumulation of debris during the scratch test.

Table 2
Young's modulus and hardness of the anodized titanium samples (*AP20*, *AP30*) and the bare material.

	E (GPa)	H (GPa)
Ti-cp	110 ± 4	2.3 ± 0.2
AP20	140 ± 30	5.8 ± 2.2
AP30 rosettes	150 ± 12	6.5 ± 2.1
AP30 phosphates	30 ± 12	1.9 ± 0.4

Critical load to produce the failure of the film was not observed in any of the samples, however permanent plastic deformation was observed. A very ductile behavior and very good adhesion could be seen in scratch tests performed with increasing load from 0 to 200 mN in all samples. Fig. 10 shows some elastic recovery of the *AP 20* (25%) after scratch application, implying a degree of elastic–plastic character of the samples with higher amount of phosphates on the surface. Adhesion cannot be quantified using this maximum applied load since there are no breakdown events (*i.e.* a discontinuity in the load–penetration of the scratch essays), due to the absence of delamination or debonding of the anodic films.

The *AP30* sample presented a very rough surface due to the presence of the titanium oxide deposits, as it was illustrated with SEM images and with the Ra values. This is why the pre-scan showed a heterogeneous surface, and also why the scratch presents the same tendency. The influence of the initial roughness is very important for the deposit adhesion but also for comparing with the starting surface condition. Almost identical behavior was observed for both samples, not showing any signs of cracks and delamination, which underline their ductile behavior.

The coefficient of friction (COF) of the anodized samples presented different values: 0.19 for *AP20* and 0.28 for *AP30*, with less than a 10% error, as can be seen at the bottom of each graph in Fig. 10. The values were taken for the early stages of the COF *vs.* scratch displacement curve and after the first 100 µm of stabilization. The COF values are in all cases very stable in the applied load range, showing good adhesion to the metallic substrate. The difference in the COF values between the *AP30* and the *AP20* is due to the irregularity of this sample, as seen before. These values show correspondence with the nanoscratch behavior explained before.

4. Conclusions

X-ray photoelectron spectroscopy and Raman spectroscopy techniques showed the presence of phosphor compounds on the treated

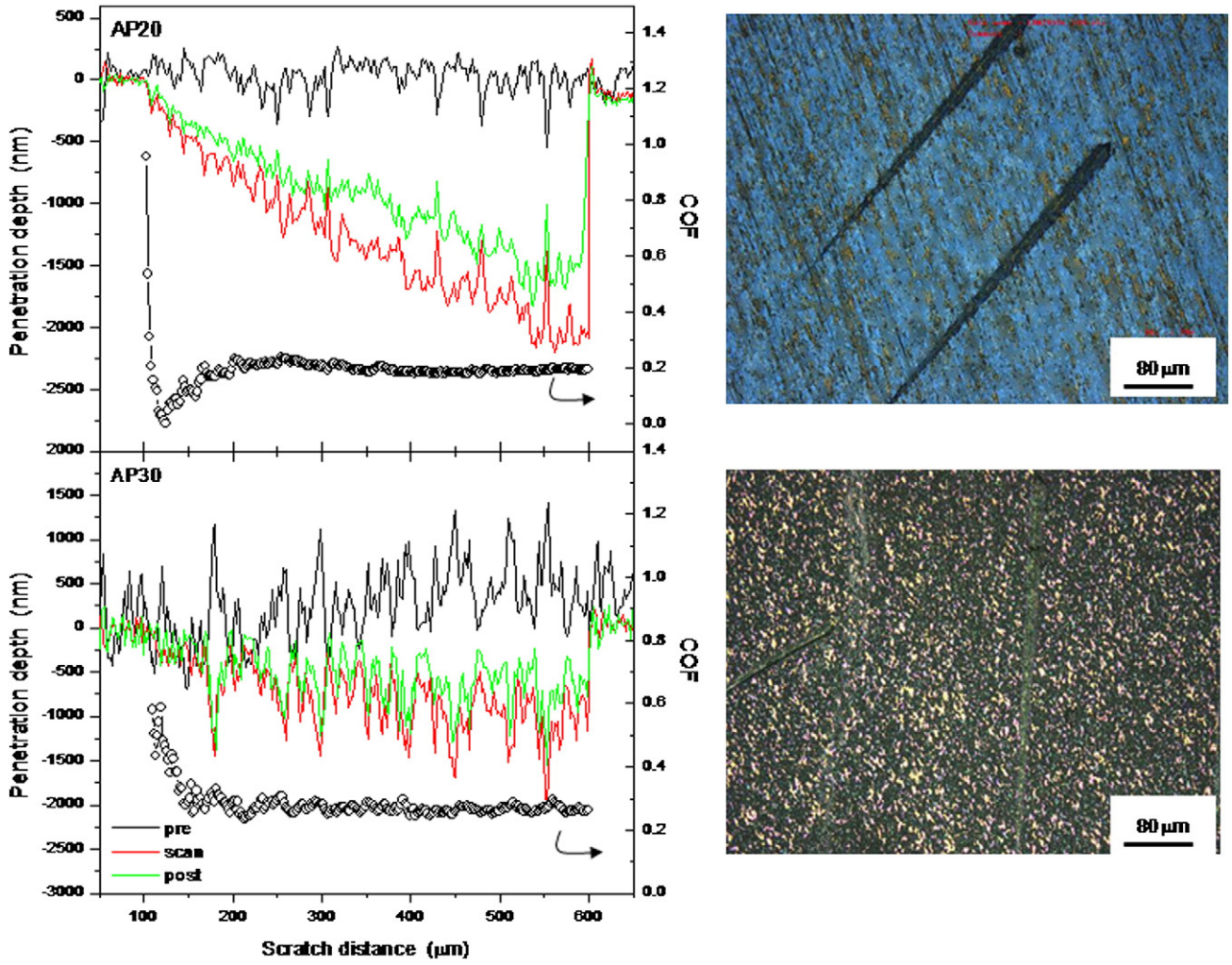

Fig. 10. Scratch depth profile as a function of the scratch displacement of the indenter tip of the anodized samples (*AP20* and *AP30*). The pre-scan, scan and post-scan made are shown. On the bottom of each graph, the coefficient of friction (COF) as a function of increasing scratch distance is also shown. Optical microscopy of the scratched surfaces of the *AP20* and *AP30* samples are shown at the right side of the figure.

surfaces. By means of Raman spectroscopy it was also possible to observe the presence of titanium dioxide as anatase in the main crystalline phase.

Anodized samples presented less passivity current density respect to the bare substrate, showing that the anodic film acts as an effective barrier to the electrolyte entrance to reach the metallic surface.

Mechanical properties of bare substrate were improved with the formation of anodic films. The hardness value was increased in the rosettes zones and the Young's modulus was decreased in the phosphor-compounds-rich's zones on the *AP30* sample, generating an interface with different elastic properties that could enhance the prosthesis performance.

Nano-scratch tests showed a very ductile behavior and good adhesion of anodic films, without any apparent signs of cracks or delamination.

Acknowledgments

The authors would like to thank the National Research Council of Argentina (CONICET), National Agency for Science and Technology Promotion (ANPCyT–PICT 00550 and PICT 0917) and National University of Mar del Plata (UNMdP-15/G270) for financial support.

References

[1] J.J. Jacobs, M.D. Jeremy, J.L. Gilbert, R.M. Urban, J. Bone Joint Surg. 80 (1998) 268.
[2] M. Bowditch, R. Villar, J. Bone Joint Surg. Br. 83-B (2001) 680.
[3] X. Liu, P.K. Chu, C. Ding, Mater. Sci. Eng. Rep. 47 (2004) 49.
[4] P. Tengvall, I. Lundström, Clin. Mater. 9 (1992) 115.
[5] Y.T. Sul, P. Johansson, B.S. Chang, E.S. Byon, Y. Jeong, J. Appl. Biomater. Biomech. 3 (2005) 18.
[6] Y.T. Sul, C.B. Johansson, Y. Kang, D.G. Jeon, T. Albrektsson, Clin. Implant Dent. Relat. Res. 4 (2002) 78.
[7] Y.T. Sul, C. Johansson, A. Wennerberg, L.R. Cho, B.S. Chang, T. Albrektsson, Int. J. Oral Maxillofac. Implants 20 (2005) 349.
[8] D. Gong, C.A. Grimes, O.K. Varghese, W. Hu, R.S. Singh, Z. Chen, E. Dickey, J. Mater. Res. 16 (2001) 3331.
[9] S. Karuppuchamy, J.M. Jeong, Mater. Chem. Phys. 93 (2005) 251.
[10] H.-J. Oh, J.-H. Lee, Y. Jeong, Y.-J. Kim, C.-S. Chi, Surf. Coat.Technol. 198 (2005) 247.
[11] H.-J. Song, S.-H. Park, S.-H. Jeong, Y.-J. Park, J. Mater. Process. Technol. 209 (2009) 864.
[12] G.A. Crawford, N. Chawla, K. Das, S. Bose, A. Bandyopadhyay, Acta Biomater. 3 (2007) 359.
[13] A.F. Yetim, Surf. Coat.Technol. 205 (2010) 1757.
[14] H.H. Park, I.S. Park, K.S. Kim, W.Y. Jeon, B.K. Park, H.S. Kim, T.S. Bae, M.H. Lee, Electrochim. Acta 55 (2010) 6109.
[15] B. Yang, M. Uchida, H.-M. Kim, X. Zhang, T. Kokubo, Biomaterials 25 (2004) 1003.
[16] R. Beranek, H. Hildebrand, P. Schmuki, Electrochem. Solid-State Lett. 6 (2003) B12.
[17] Y.-T. Sul, C. Johansson, K. Röser, T. Albrektsson, Biomaterials 23 (2002) 1809.
[18] L.L. Hench, J. Wilson, in: Wilson (Ed.), Advanced Series in Ceramics — World Scientific Hench, vol. I, 1993.
[19] G. Wei, B. Bhushan, S.J. Jacobs, Ultramicroscopy 100 (2004) 375.
[20] S. Simunková, O. Bláhová, I. Stepánek, J. Mater. Process. Technol. 133 (2003) 189.
[21] L.-Y. Huang, J.-W. Zhao, K.-W. Xu, J. Lu, Diamond Relat. Mater. 11 (2002) 1454.
[22] X. Li, F. Huang, M. Curry, S.C. Street, M.L. Weaver, Tribol. Lett. 19 (2005) 273.
[23] J. Ballarre, E. Jimenez-Pique, M. Anglada, S. Pellice, A.L. Cavalieri, Surf. Coat.Technol. 203 (2009) 3325.
[24] F. Moulder, W.F. Stickle, P.E. Sobol, K.D. Bomben, Physical Electronics, Inc. Eden Praire, Minnesota 55344, USA (1995).

[25] T. Kokubo, S. Ito, Z.T. Huang, T. Hayashi, S. Sakka, T. Kitsugi, T. Yamamuro, J. Biomed. Mater. Res. 24 (1990) 331.
[26] W.C. Oliver, G.M. Pharr, J. Mater. Res. 7 (1992) 1564.
[27] T.W. Scharf, J.A. Barnard, Thin Solid Films 308–309 (1997) 340.
[28] K.S. Raja, M. Misra, K. Paramguru, Electrochim. Acta 51 (2005) 154.
[29] J. Choi, R.B. Wehrspohn, J. Lee, U. Gasele, Electrochim. Acta 49 (2004) 2645.
[30] K. Lu, Z. Tian, J.A. Geldmeier, Electrochim. Acta 56 (2011) 6014.
[31] T. Shibata, Y.-C. Zhu, Corros. Sci. 37 (1995) 133.
[32] Y.-T. Sul, C.B. Johansson, S. Petronis, A. Krozer, Y. Jeong, A. Wennerberg, T. Albrektsson, Biomaterials 23 (2002) 491.
[33] X. Cui, H.-M. Kim, M. Kawashita, L. Wang, T. Xiong, Dent. Mater. 25 (2009) 80.
[34] T. Shibata, Y.-C. Zhu, Corros. Sci. 37 (1995) 253.
[35] R. Ciceo Lucacel, M. Maier, V. Simon, J. Non-Cryst. Solids 356 (2010) 2869.
[36] C.E.B. Marino, P.A.P. Nascente, S.R. Biaggio, R.C. Rocha-Filho, N. Bocchi, Thin Solid Films 468 (2004) 109.
[37] K. Mori, K. Maki, S. Kawasaki, S. Yuan, H. Yamashita, Chem. Eng. Sci. 63 (2008) 5066.
[38] W.-Y. Chang, T.-H. Fang, Z.-W. Chiu, Y.-J. Hsiao, L.-W. Ji, Microporous Mesoporous Mater. 145 (2011) 87.
[39] J.M. Macak, H. Tsuchiya, L. Taveira, A. Ghicov, P. Schmuki, J. Biomed. Mater. Res. 75A (2005) 928.
[40] B.N. Lucas, C.T. Rosenmayer, W.C. Oliver, Mater. Res. Soc. Symp. Proc. 505 (1998) 97.
[41] A.C. Fischer-Cripps, Surf. Coat.Technol. 200 (2006) 4153.